



Research article

Thermally-induced color transformation of hematite: insight into the prehistoric natural pigment preparation



Nadya Nurdini^a, Moh. Mualliful Ilmi^a, Evi Maryanti^{a,b}, Pindi Setiawan^c, Grandprix Thomryes Marth Kadja^{d,e,*}, Ismunandar^{a,**}

^a Division of Inorganic and Physical Chemistry, Institut Teknologi Bandung, Jl. Ganesha No. 10, Bandung 40132, Indonesia

^b Department of Chemistry, Universitas Bengkulu, Jl. W.R. Supratman, Bengkulu 38371, Indonesia

^c Division of Visual Communication and Multimedia, Institut Teknologi Bandung, Jl. Ganesha No. 10, Bandung 40132, Indonesia

^d Research Center for Nanosciences and Nanotechnology, Institut Teknologi Bandung, Jl. Ganesha No. 10, Bandung 40132, Indonesia

^e Center for Catalysis and Reaction Engineering, Institut Teknologi Bandung, Jl. Ganesha No. 10, Bandung 40132, Indonesia

ARTICLE INFO

Keywords:

Hematite
Pigment
Rock art
Thermal transformation
Structure transformation

ABSTRACT

Since the prehistoric era, hematite has been known as a reddish color pigment on rock art, body paint, and decorating substances for objects discovered almost worldwide. Recently, studies about purple hematite used in prehistoric pigment have been done vigorously to investigate the origin of the purple pigment itself. These previous studies indicate that the differentiation of crystallinity, crystal size, morphology, and electronic structure can cause the color shift, resulting in purple hematite. In this study, we conducted a detailed study of the sintering temperature effects on the formation of hematite minerals. This study aims to reveal the structural, crystallography, and electronic transformation in hematite due to heating treatment at various temperatures. The hematite was synthesized using precipitation to imitate the primary method of hematite formation in nature. The sintering process was carried out with temperature variations from 600 °C to 1100 °C and then characterized by crystallographic and structural properties (XRD, Raman Spectroscopy, FTIR), particle size (TEM), as well as electronic properties (DRS, XANES). The crystallinity and particle size of hematite tend to increase along with higher sintering temperatures. Moreover, we noted that the octahedral distortion underwent an intensification with the increase in sintering temperature, which affected the electronic structure of hematite. Specifically, the $1s \rightarrow 3d$ transition exhibited lower energy for hematite produced at a higher temperature. This induced a shift in the absorbed energy of the polychromatic light that led to a color shift within hematite, from red to purple. Our finding emphasizes the importance of electronic structure in explaining hematite pigment's color change rather than relying on simple reasons, such as particle size and crystallinity. In addition, this might strengthen the hypothesis that the prehistoric human created a purple hematite pigment through heating.

1. Introduction

Ochre has been a favored material as a pigment since the prehistoric era. Ochre contained clay and silica with various types of iron minerals. These types of iron minerals in ochres produce a range of colors, from yellow, α -FeOOH—goethite (Longa-Avello et al., 2017; Mondragón et al., 2019; Salomon et al., 2012), brown, γ -Fe₂O₃—maghemite (Cornell and Schwertmann, 2003), red, α -Fe₂O₃—hematite, and purple, α -Fe₂O₃—hematite or KFe₃(SO₄)₂(OH)₆—jarosite (Hunt et al., 2016; Huntley et al., 2015; Ilmi et al., 2020; Kurniawan et al., 2019; Nurdini

et al., 2020). In addition, other colors in rock art images, such as black, contain manganese oxide or charcoal (McPeak et al., 2013; Chalmin et al., 2003, 2004, 2006), while white contains Al₂O₃ 2SiO₂·2H₂O—kaolinite, Mg₃Ca(CO₃)₄—huntite (Huntley et al., 2014), CaSO₄·2H₂O—gypsum or CaCO₃—calcite (Ilmi et al., 2021a). Among all the natural minerals that have been mentioned, red ochre, which contains hematite, is the most widely used natural material as a pigment in prehistoric rock art around the world.

The formation of ochre occurred through the aerobic natural weathering of iron-bearing minerals (Miot and Etique, 2016).

* Corresponding author.

** Corresponding author.

E-mail addresses: grandprix.thomryes@itb.ac.id (G.T.M. Kadja), ismu@chem.itb.ac.id (Ismunandar).

Furthermore, the formation of the mineral hematite in red ochre can go through several other processes, such as the hydrolysis of a solution of 2-line ferrihydrite (Heaney et al., 2020), solid-state transformation at high temperatures from iron hydroxide, oxidation of Fe^{2+} (magnetite and maghemite), and the thermal decomposition of iron salts (Cornell and Schwertmann, 2003). Utilization of natural pigments, especially ochre, has been practiced by the direct ancestor of modern humans (*Homo sapiens sapiens*) on various occasions, such as wall paintings, funerary contexts, and ceramic artifacts (Chalmin and Huntley, 2018; Elias et al., 2006; Iriarte et al., 2009). In Indonesia, the discovery of the rock art of wild Bovid from Kalimantan and the hunting scene of therianthropes from Sulawesi revealed that red ochre (hematite) was used from at least 43,000–40,000 years ago based on the U-Th series dating (Aubert et al., 2018, 2019). This rock art is currently the oldest found artwork depicting hunting activities in the world (Ilmi et al., 2021b). In addition, Studies on prehistoric rock art exhibit the purple color of hematite alongside the red color in several sites, such as in Australia and Indonesia (Huntley et al., 2015; Hunt et al., 2016; Kurniawan et al., 2019; Ilmi et al., 2020; Nurdini et al., 2020). Previous studies stated that elements composition and particle size are different between purple and red hematite (Cornell and Schwertmann, 2003; Marshall et al., 2005; Opuchovic and Kareiva, 2015).

Hematite has been known to have rhombohedral symmetry with $R\bar{3}c$ space group with hexagonal close-packed (hcp) oxygen sheet and octahedral interstices between the sheet of Iron (Kubáňová et al., 2019; Xu et al., 2015). On the other hand, purple hematite was reported to have a larger particle size, higher crystallinity, and distorted symmetry of octahedral (Castagnotto et al., 2021; de Oliveira et al., 2002; Ilmi et al., 2020; Mastrotheodoros et al., 2010; Nurdini et al., 2020). These

discrepancy characteristics of hematite are induced by optical spectrum shift absorbed by materials, thus resulting in hematite with purple color. This phenomenon can be occurred either naturally and/or synthetically (Faivre, 2016). Previous research's hypotheses stated that purple hematite on prehistoric rock art is formed due to the heat treatment of red hematite, thus changing the size and structural properties, albeit the hypothesis has not been proven (Ilmi et al., 2020; Nurdini et al., 2020). Meanwhile, research on natural pigments purple (Caput mortuum) by Castagnotto et al. (2021) explained that natural pigment (hematite purity < 80%) cannot change then produce a purple color, and only pure hematite can obtain purple color due to heat treatment. However, a more detailed explanation regarding the color change of the hematite pigment from red to purple, other than differences in grain size, has not been obtained and understood.

Thus, this study will explain the effect of heat treatment on changes, especially in crystallographic and electronic properties, along with the particle size of hematite and its effect on color shift. This research was conducted by laboratory-scale hematite synthesized using the precipitation method. The obtained hematite was treated with various calcination temperatures to understand the effect of temperature on the crystalline structure of the hematite and then generate color changes. The precipitation method in the synthesis of hematite can produce a relatively small particle size (<1 μm) and a more uniform size (Pomiès et al., 1999; Bora et al., 2013). Furthermore, the precipitation method forms hematite as the most stable mineral that occurs naturally, then used as a natural pigment. The results of this study are expected to provide comprehensive information about the effect of heating on color change, especially hematite, which was used as a pigment for prehistoric images. On top of that, this study envisioned pre-treatment of hematite from a natural

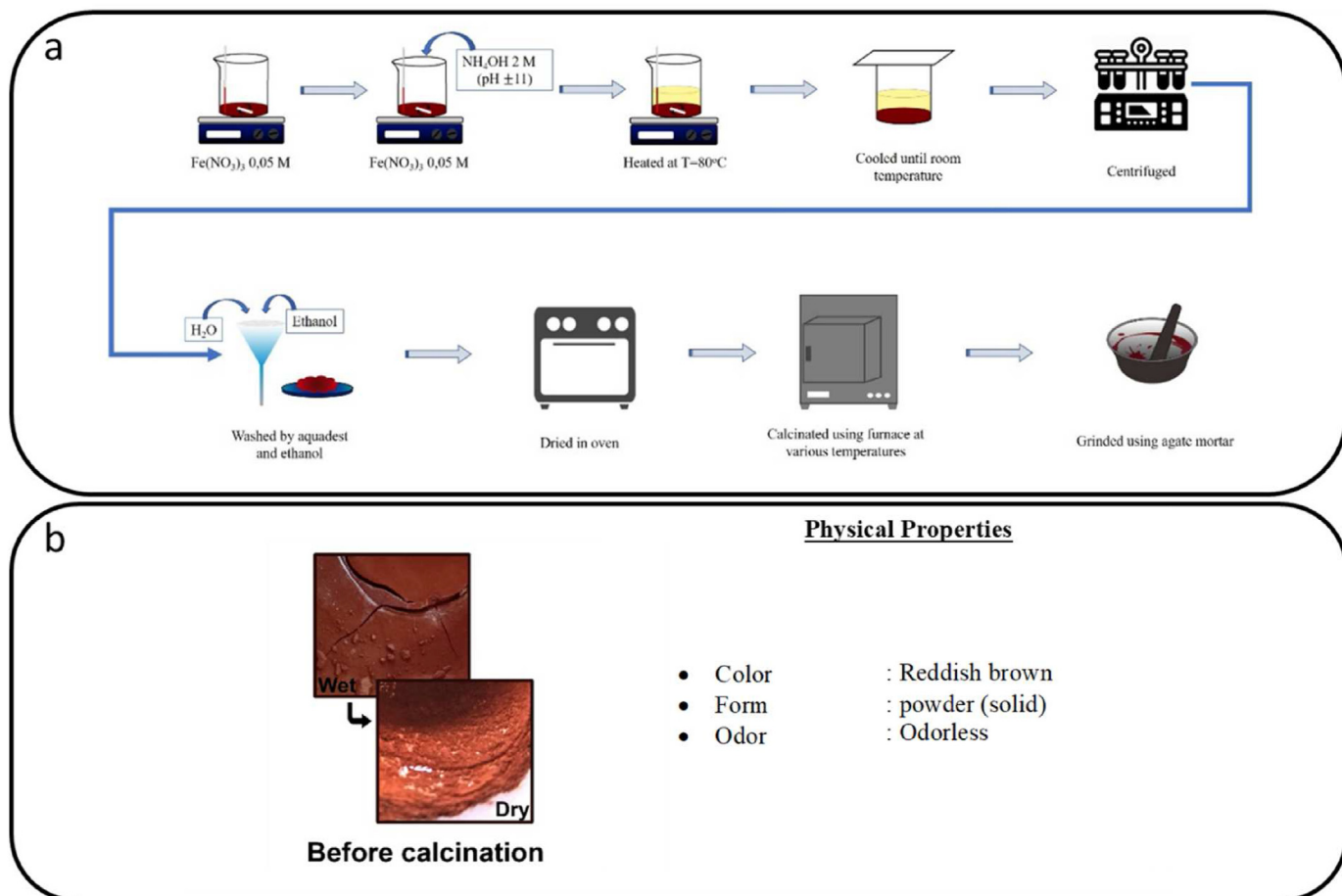


Figure 1. (a) The scheme of hematite synthesis using precipitation method, and (b) Physical properties of samples after precipitation phase.

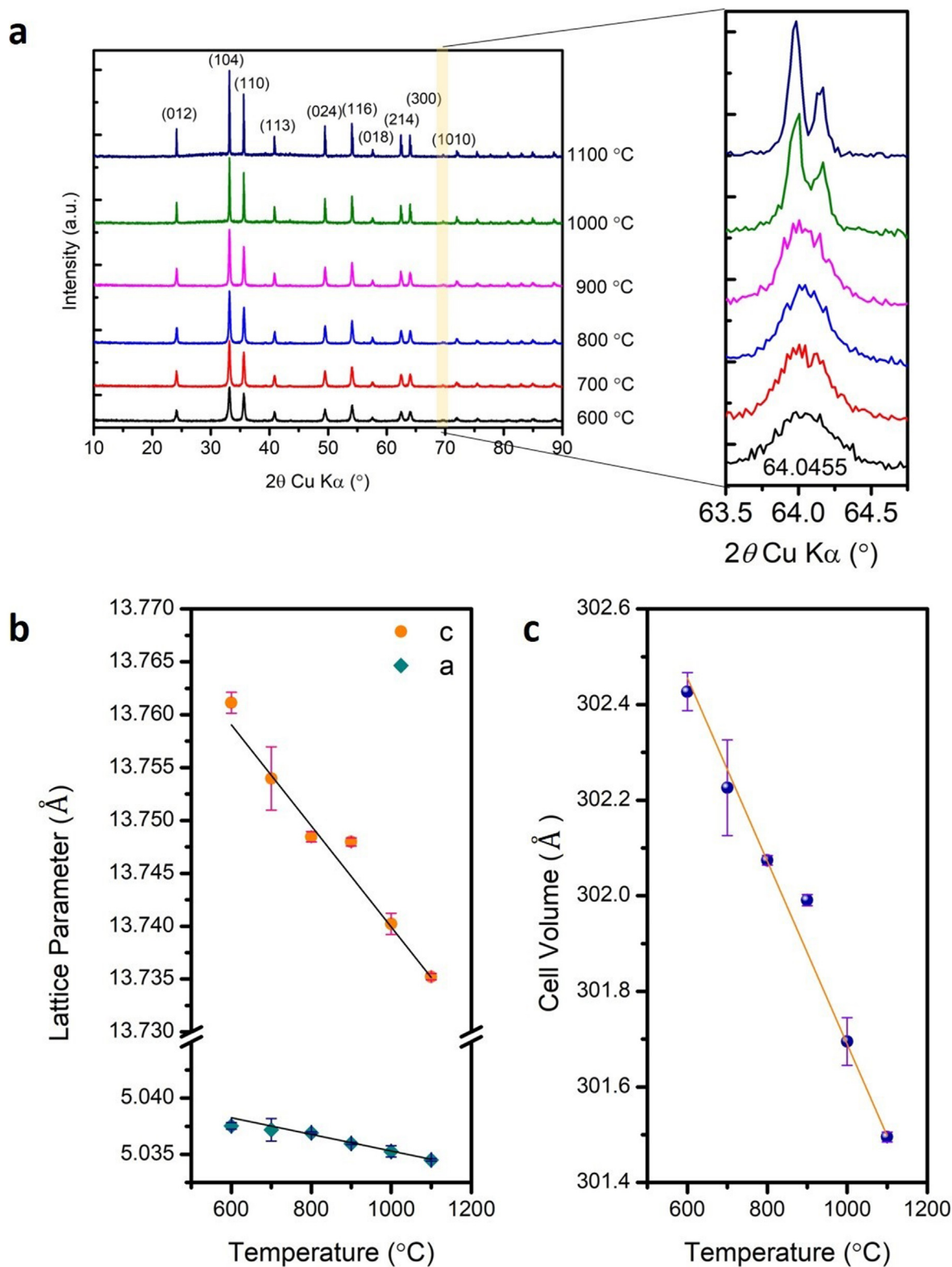


Figure 2. (a) XRD patterns of hematite calcined at 600 °C–1100 °C. The sample with a higher calcination temperature has a sharper peak and higher intensities that indicate the crystalline phase increase than samples with a lower calcination temperature. (b) Cell parameters (a and c) with (c) Cell volume of calcinated samples at various temperatures between 600 °C and 1100 °C that obtained by Rietveld refinement. The observed data represent cell parameter values were decreased along with calcined temperature increases.

Table 1. The calculated crystallite size of samples using Scherrer equation on preference peak (104) with the cell parameters, crystallinity, and cell volume of samples obtained by Rietveld refinement using Rietica.

T (°C)	D (Å)	Crystallinity (%)	a, b (Å)	c (Å)	Cell Volume (Å ³)	Rp (%)	Rwp (%)
1100	115.03 (1)	100.00	5.0345 (1)	13.7352 (3)	301.50 (1)	13.44	11.89
1000	56.468 (2)	88.67	5.0353 (5)	13.740 (1)	301.70 (5)	13.15	11.79
900	35.890 (3)	70.60	5.0359 (1)	13.7485 (4)	301.99 (1)	12.39	9.59
800	31.922 (3)	61.00	5.0369 (1)	13.7485 (5)	302.07 (1)	12.59	9.75
700	27.627 (3)	59.06	5.037 (1)	13.754 (3)	302.2 (1)	12.43	10.12
600	22.528 (4)	55.90	5.0374 (3)	13.761 (1)	302.37 (4)	13.51	12.51

T: Temperature (°C).

D: Crystallite size (Å).

a,b,c: Lattice parameter (Å).

Rp: Profile R-factor.

Rwp: Weight profile R-factor in.

source before heat treatment and technological developments in the prehistoric era.

2. Material and methods

2.1. Materials

The synthesis path of hematite was conducted by the precipitation method employed by Lassoued (Lassoued et al., 2017, 2018). The reagents were Fe(NO₃)₃·6H₂O as a precursor, ammonia solution (NH₄OH) as a precipitating agent, and ethanol to rinse the precipitation. All reagent was purchased from Merck and used without further purification.

2.2. Synthesis procedure

Figure 1a exhibits the illustration of the synthesis procedure. First, Fe(NO₃)₃·6H₂O solution (0.05 M) was heated at 80 °C, then added ammonia solution (NH₄OH) dropwise while stirring thoroughly at the constant temperature. Next, the solution was stirred for 3 h and cooled down until room temperature. Figure 1b shows the precipitate as a red-brown precipitate. Afterward, the precipitates were gathered using a centrifuge at 4000 rpm for 15 min. Next step, all solid substances were washed with distilled water and dried at 110 °C for 24 h in the oven. Then, the sample was calcinated for 4 h at temperatures between 600 °C and 1100 °C in an Air atmosphere. Finally, the samples were collected and ground using agate mortar until a fine powder was established.

2.3. Characterization

The crystalline phase of samples was characterized by X-Ray Diffraction (XRD) using Bruker D8 Advance with Cu K α radiation ($\lambda = 1.5418 \text{ \AA}$). The measurement data was collected at 20 from 10° to 90° with 0.002°/s scan step mode. Before the measurement, all samples were ground to form a fine powder. The diffractogram was analyzed to identify the characteristic of the crystal phase, then compared with references using Highscore PAN Analytical (standard ICDD card no. 33-0664). The diffraction pattern was refined using Rietica to identify samples' lattice parameters.

Raman spectroscopy was employed to investigate the mineral composition based on the typical chemical bonding of the samples. Raman spectra were measured using the Bruker Senterra instrument with a 785 nm excitation, the power output of 20 mW, and spectral resolution of 4 cm⁻¹. In addition, the Fourier Transform Infrared (FTIR) spectra of samples were recorded by Shimadzu Prestige FTIR spectrometer using the KBr pellet method. The measurement was conducted between 400 cm⁻¹ and 4000 cm⁻¹ with a resolution of 4 cm⁻¹.

The particle size and shape of hematite were observed using Hitachi TEM HT7700. The observation was conducted with accelerated voltage 120 kV and 50,000 \times magnification. In addition, evolution™ 201/220

UV-Visible Spectrophotometers performed the spectra reflectance of hematite at wavelengths 400 nm–900 nm.

Identification of the hematite phase (α -Fe₂O₃) and the electronic properties was employed using Fe K-edge X-ray Absorption Near-Edge Structure (XANES) in fluorescence detection mode under ambient air conditions using synchrotron radiation source at Synchrotron Light of Research Institute (SLRI), Thailand. The measurements were recorded using a Ge detector in the energy range of 7112 eV with five eV/s of step size. The measurement process was conducted using a 6 μm thickness of polypropylene sample container. The results in the form of spectra are processed using Athena software to remove the background, performed normalization and calculation using the Linear Combination Fittings to determine the mineral phase of Fe, thus compared with reference spectra of standard hematite (α -Fe₂O₃) (Ravel and Newville, 2005).

3. Results

3.1. X-ray diffraction (XRD)

The crystalline phase and the purity of hematite were determined using X-ray diffraction. Figure 2a presents the diffraction pattern of samples under six calcination temperatures between 600 °C and 1100 °C with an interval of 100 °C. According to the hematite database, ICDD card standard no. 33-0664, all peaks showed the plane of pure hematite (α -Fe₂O₃) that possesses a rhombohedral structure with an $\bar{R}\bar{3}c$ space group at (012), (104), (110), (113), (024), (116), (018), (214), (300), and (1010) (Almeida et al., 2009; Rafi et al., 2015; Zhang et al., 2013; Morales-Morales, 2017; Tadic et al., 2019). These patterns indicate that only α -Fe₂O₃ is formed at calcination temperatures between 600 °C and 1100 °C with no other mineral phases detected. Meanwhile, if the synthesis is carried out at a temperature below 600 °C, it shows the formation of other iron compounds such as ferrihydrite, goethite (Rout et al., 2014), and maghemite (γ -Fe₂O₃) (Rafi et al., 2015; Morales-Morales, 2017).

Observation of the diffraction pattern in Figure 2a showed that the peaks at the diffractogram of samples escalated and narrowed as the temperature increased as α -Fe₂O₃ without other iron phases detected. Equation (Eq. (1)) presented the Scherrer formula that exhibits the relation between the FWHM (Full Width at Half Maximum) value and the level of crystallinity and crystallite size (Rout et al., 2014).

$$D = \frac{K\lambda}{\beta \cos\theta} \quad (1)$$

D symbolizes the mean of crystallite size, K is the shape factor constant that varies with the crystallite shape, λ is X-ray wavelength, β is Full Width at Half-Maximum (FWHM), and θ is Bragg's angle. Thus, the sample's crystallite size was estimated by calculating using the Scherrer equation based on preference orientation peak (104). The calculated crystallite size presented in Table 1 exhibits the greater crystallite formed

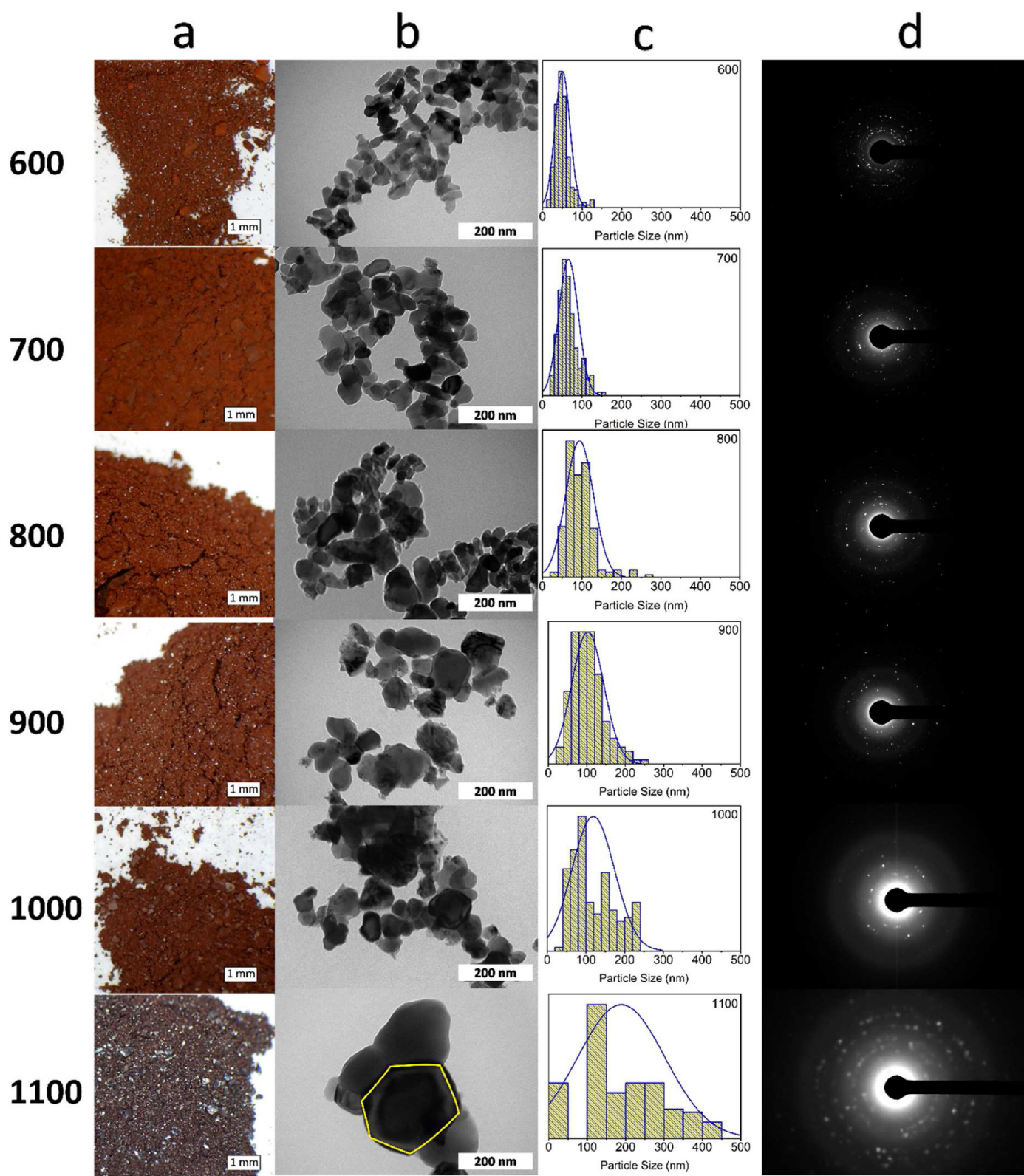


Figure 3. (a) Optical appearances, (b) TEM images of hematite at various calcined temperatures (°C) with (c) the histogram of respective particle sizes, and (d) the SAED pattern of each sample. Higher calcined temperature presents an image with a hexagonal shape with a more prominent and denser crystal than hematite that was calcined at a lower temperature.

Table 2. Average particle size value of hematite synthesized with precipitation method at various temperatures of calcination.

Temperature (°C)	600	700	800	900	1000	1100
Particle Size (nm)	50 ± 18	66 ± 24	94 ± 35	103 ± 41	119 ± 55	189 ± 69

at the high calcination temperature. Therefore, the Crystallite size can be predicted through peak sharpness.

If the diffractogram was enlarged (Figure 2a), the sharpened peak at the high calcination temperature also generates the splitting peak of $K\alpha_1$ and $K\alpha_2$. In contrast, the splitting peak of $K\alpha_1$ and $K\alpha_2$ in lower

temperatures of calcination was not detected since the peak was broader; thus the $K\alpha_1$ and $K\alpha_2$ were merged in one peak. As we know, the characteristic x-ray diffraction spectrum consists of $K\alpha_1$, $K\alpha_2$ and $K\beta$ radiation with a peak intensity ratio of 1:0.5:0.25, respectively. $K\beta$ is generally removed using a monochromator to avoid errors in data interpretation.

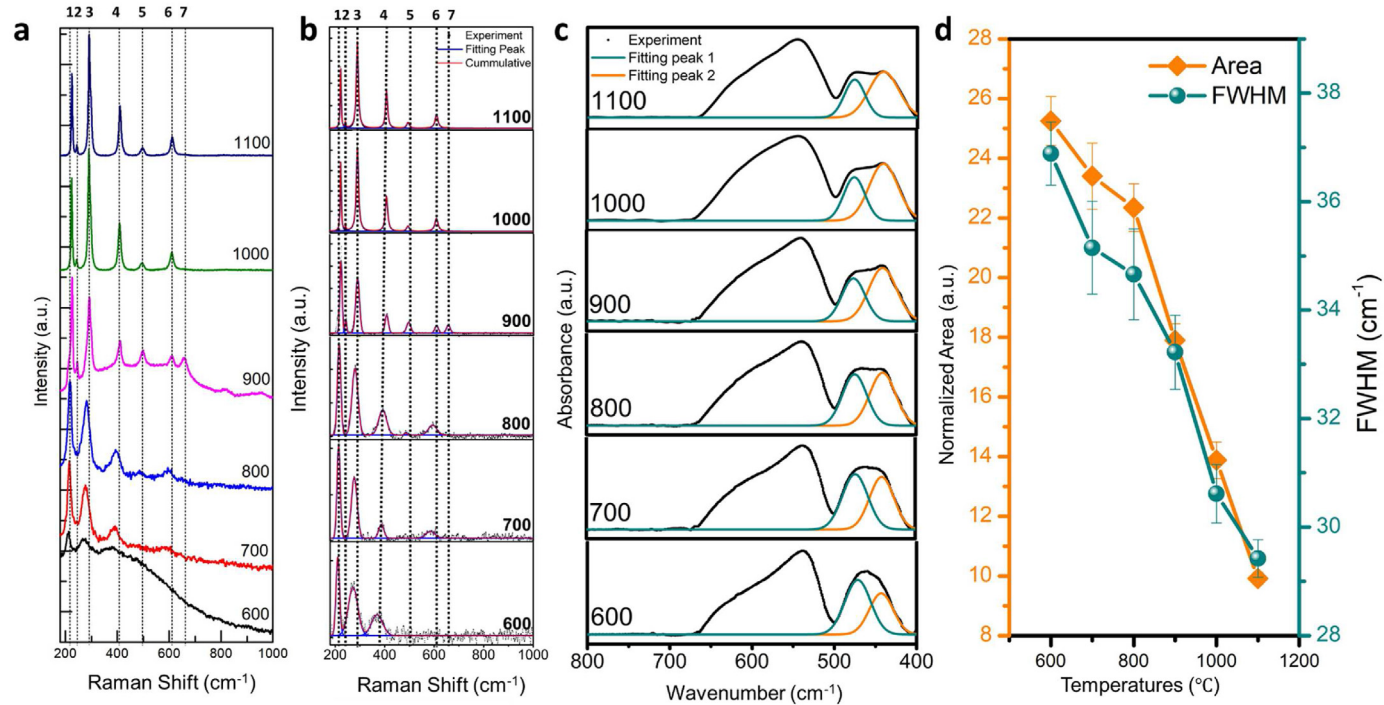


Figure 4. (a) Spectrum of Raman shift and (b) Fitting peak of spectra of Raman spectroscopy from 50 cm^{-1} to 1000 cm^{-1} of hematite calcinated at $600 \text{ }^{\circ}\text{C}$ – $1100 \text{ }^{\circ}\text{C}$. The spectrum of hematite calcined at lower temperatures has fewer and broader peaks than hematite that calcined at a higher temperature, indicating that the crystallinity of hematite increases within higher temperatures. (c) FTIR spectra of hematite synthesized at calcination temperature $600 \text{ }^{\circ}\text{C}$ – $1100 \text{ }^{\circ}\text{C}$ with the fitting curve at $\sim 440 \text{ cm}^{-1}$ – 470 cm^{-1} using Gaussian of E_u vibration with (d) normalized peak area and FWHM value at 470 cm^{-1} .

Table 3. Raman shift and FWHM values of hematite at $600 \text{ }^{\circ}\text{C}$ – $1100 \text{ }^{\circ}\text{C}$ (Fouad et al., 2019; Jubb and Allen, 2010; Kurniawan et al., 2019; Mansour et al., 2017; Marshall et al., 2020).

T (°C)	Raman Mode (cm^{-1})						
	1 $A_{1g}(1)$	2 $E_g(1)$	3 $E_g(2)$	4 $E_g(3)$	5 $A_{1g}(2)$	6	7 1LO E_u
600	Raman Shift	210.8 (9)		272.5 (4)	369.4 (5)		
	FWHM	17.1 (4)		45.5 (1)	52.9 (4)		
700	Raman Shift	214.7 (2)		277.9 (1)	386.9 (3)		584.9 (8)
	FWHM	15.3 (5)		27.1 (8)	24.2 (8)		43.8 (5)
800	Raman Shift	216.6 (3)		280.6 (2)	392.2 (5)	485.9 (7)	593.6 (1)
	FWHM	16.2 (2)		28.4 (6)	37.9 (5)	11.9 (5)	40.1 (9)
900	Raman Shift	224.7 (7)	244.2 (2)	291.7 (2)	408.9 (9)	497.5 (7)	609.6 (7)
	FWHM	10.9 (7)	7.8 (5)	18.4 (2)	15.8 (5)	19.7 (4)	16.8 (5)
1000	Raman Shift	223.9 (2)	243.1 (2)	291.2 (2)	408.6 (1)	495.0 (4)	609.7 (1)
	FWHM	5.0 (1)	3.7 (5)	10.3 (1)	11.3 (1)	13.6 (1)	15.0 (5)
1100	Raman Shift	225.02 (2)	244.0 (2)	292.20 (2)	410.17 (5)	496.8 (4)	611.4 (2)
	FWHM	4.69 (6)	3.4 (4)	9.45 (6)	9.9 (1)	13.0 (1)	13.6 (5)
Notes	Hematite	Hematite	Hematite	Hematite	Hematite	Hematite	Crystal disorder

The number in parentheses indicated the error value of each data.

Table 4. Fitting curve result of hematite peak of Eu vibration at FTIR using Gaussian fitting.

T (°C)	Fitting peak 1 (Core)			Fitting peak 2 (Shell)		
	Wavenumber	Area	FWHM	Wavenumber	Area	FWHM
600	471.4 (5)	25.2 (8)	36.8 (6)	443.9 (5)	17.7 (8)	34.3 (5)
700	472.3 (5)	23 (1)	35.1 (8)	443.8 (7)	19 (1)	35.0 (6)
800	474.6 (2)	22.3 (8)	34.6 (8)	441.6 (3)	24.3 (5)	36.6 (4)
900	476.4 (2)	17.8 (5)	33.2 (7)	441.0 (3)	26.6 (4)	39.8 (4)
1000	475.5 (2)	13.8 (6)	30.6 (5)	440.0 (2)	24.6 (3)	41.3 (4)
1100	476.0 (2)	9.9 (2)	29.4 (3)	440.6 (2)	17.3 (2)	42.5 (4)

Meanwhile, $K\alpha_2$ radiation which is only 0.004° different from $K\alpha_1$ is generally not visible due to overlapping. However, the $K\alpha_2$ peak can increase the error rate in determining the FWHM value or crystal size because it produces a 'tail' at the peak (asymmetric peak). From this explanation, the splitting that appears on the sample diffractogram with a high heating temperature ($1000\text{ }^\circ\text{C}$ – $1100\text{ }^\circ\text{C}$) results in the calculation of FWHM and crystal size with a lower error rate (Parrish and Langford, 2006; Rachinger, 1948).

Further analysis of the diffractogram was carried out by Rietveld refinement using Rietica to obtain parameter lattice (a , b , c) and cell volume values. Based on the Rietveld refinement results (Table 1), cell parameters c changed significantly compared with cell parameters a and b (Figure 2b and c). These trends exhibit the relation of calcined temperature with the lattice parameter function of hematite. Samples with higher calcination temperatures will have a smaller lattice parameter value, resulting in a contraction of the hematite unit cell (Sorescu and Xu, 2012).

3.2. Transmission electron microscopy (TEM)

The detailed shape and particle size of samples were identified by TEM characterization. Figure 3a presented the differences in the hematite color at various calcined temperatures. The hematite with lower calcined temperatures tends to generate red, while higher calcined temperatures have dark red to purple color. Based on the results of TEM observation in Figure 3b, the particle size of samples synthesized at various temperatures between $600\text{ }^\circ\text{C}$ and $1100\text{ }^\circ\text{C}$ was increased following the increase in calcination temperature. The particles are smaller and more transparent at lower calcined temperatures, while higher temperatures produce larger and denser particles. Hereafter, the

particle size can be measured using ImageJ software and then plotted as a histogram with a normal distribution curve (Figure 3c). Based on the calculated particle size, it was found that the average sizes of the six hematite synthesis samples were $50 \pm 18\text{ nm}$, $66 \pm 24\text{ nm}$, $94 \pm 35\text{ nm}$, $103 \pm 41\text{ nm}$, $119 \pm 55\text{ nm}$, and $189 \pm 69\text{ nm}$, respectively (Table 2). At lower temperatures, particles focused on forming crystal core in 2D orientation. The particles will be aggregated at higher temperatures to develop larger particles in 3D orientation and produce a denser material. Salomon et al. (2012) reported that stable combustion at temperatures higher than $850\text{ }^\circ\text{C}$ produced solid particles with no pores and generated an octahedral shape. Additional data from the selected area electron diffraction (SAED) graph in Figure 3d presented the electron diffraction pattern as concentric white spots rings. The spot patterns indicated the lattice fringes of hematite related to samples' crystallinity, exhibiting that the lattice fringes pattern and the intensity of hematite increase along with the temperature degree (Rafi et al., 2015). Therefore, The SAED data supported the XRD data that the hematite with high-temperature treatment will have higher crystallinity.

3.3. Raman Spectroscopy

Raman Spectroscopy is an analytical technique that uses the vibrational mode to obtain information about the composition of chemical compounds in the material by observing its energy shift (Moldenhauer et al., 2018). Vibration modes at the first Brillouin zone center based on crystallography characteristics of hematite were shown by Eq.(2):

$$\Gamma_{\text{vib}} = aA_{1g} + 2A_{1u} + 3A_{2g} + 2A_{2u} + 5E_g + 4E_u \quad (2)$$

where A_{1u} and A_{2u} vibration modes are optically silent, the symmetrical modes (g) are Raman active, and asymmetrical vibration modes (u) are Infrared active (Marshall et al., 2020; Jubb and Allen, 2010; Chernyshova et al., 2007). Because of the inversion center features of the rhombohedral unit cell in hematite structure, a vibration mode cannot be active at Raman and Infrared modes simultaneously.

Figure 4a presents Raman spectra of hematite calcinated between $600\text{ }^\circ\text{C}$ and $1100\text{ }^\circ\text{C}$. Building upon the peak pattern shown by the six samples, all of them showed characteristic hematite spectra. Table 3

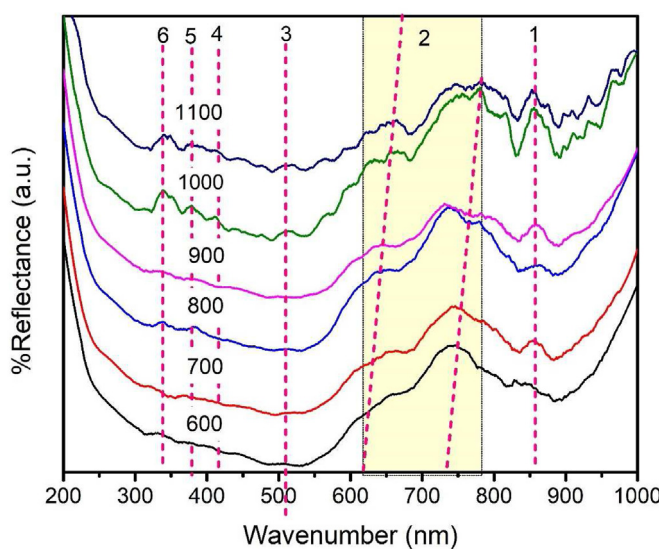


Figure 5. Diffuse Reflectance spectra of hematite calcinated at various temperatures in the UV-Visible range.

Table 5. UV-Vis DRS band position and electron transition of hematite at various temperatures of calcination.

No	Transition	Band position (nm)		
		Experiment	Cornell and Schwertmann, 2003	Sklute et al., 2017
1	${}^6A_1 \rightarrow {}^4T_1$	856	884	881
2	${}^6A_1 \rightarrow {}^4T_2$	740–780 632–663	649	672
3	$2({}^6A_1 \rightarrow {}^4T_1)$	511	529	537
4	${}^6A_1 \rightarrow {}^4E {}^4A_1$	411	404	404
5	${}^6A_1 \rightarrow {}^4E$	380	380	380
6	${}^6A_1 \rightarrow {}^4T_1$	339	319	

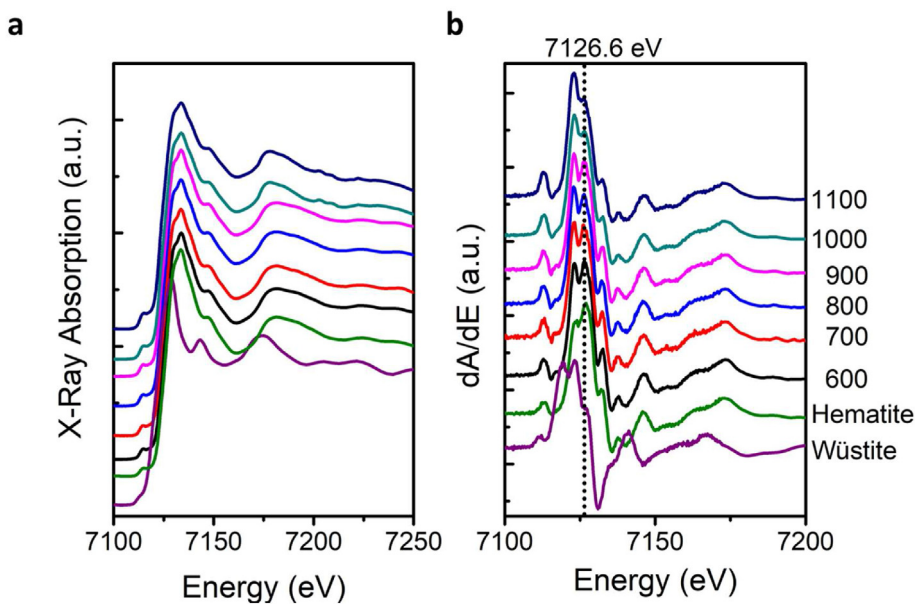


Figure 6. (a) Fe-K edge XANES spectra with (b) their first derivatives indicate that all samples have an oxidation number of Fe^{3+} .

informed the Raman Shift of the vibrational mode of each spectrum. vibrational modes were detected at $\sim 220 \text{ cm}^{-1}$ and $\sim 490 \text{ cm}^{-1}$ and vibrational modes were detected at $\sim 244 \text{ cm}^{-1}$, $\sim 290 \text{ cm}^{-1}$, $\sim 390 \text{ cm}^{-1}$, and $\sim 490 \text{ cm}^{-1}$. Spectra of hematite samples with lower calcination temperature appear only a few vibrational modes, and then the observed vibrational modes increase as long as the temperature increases.

The crystallinity of the hematite can also be observed by fitting the peaks that appear in the Raman spectra. For example, based on the FWHM value obtained (Table 3) provided by the fitting peak in Figure 4b, hematite with a higher calcination temperature has a smaller FWHM value which correlates with the high crystallinity of the hematite (Marshall et al., 2020; Kurniawan et al., 2019). Another feature that can be observed is the presence of the peak at $\sim 650 \text{ cm}^{-1}$ in 900°C that might be assigned as magnetite (Fe_3O_4) or maghemite ($\gamma\text{-Fe}_2\text{O}_3$) (Jubb and Allen, 2010; Chernyshova et al., 2007). Nevertheless, at a temperature of 900°C , they should be absent due to the thermal transformation to the hematite phase as the most stable form of iron oxide (Kinebuchi and Kyono, 2021). Thus, the presence of this peak should be assigned as longitudinal optical (LO) E_u mode of hematite originated from hematite's crystal disorder (Fouad et al., 2019; Jubb and Allen, 2010; Kurniawan et al., 2019; Mansour et al., 2017; Marshall et al., 2020).

3.4. Fourier Transform Infrared (FTIR)

The analysis of functional groups in the sample was carried out using FTIR. Based on FTIR measurement spectra (Figure 4c), all hematite samples showed absorption at wavenumbers of $\sim 450 \text{ cm}^{-1}$ and $\sim 560 \text{ cm}^{-1}$. The two wavenumbers are the typical peak of $\text{Fe}^{3+}\text{-O}$, defined as the E_u and A_{2u}/E_u vibrational mode of hematite (Chernyshova et al., 2007; Chukanov and Chervonnyi, 2016). Previous work by Chernyshova et al. (2007) emphasized that the E_u band is more stable from shape and optical effect to analyze the structural properties of hematite. As seen in Figure 4d, the peak at $\sim 450 \text{ cm}^{-1}$ changed with different calcination temperatures. Gaussian fitting at the peak presented two peaks located at $\sim 440 \text{ cm}^{-1}$ and $\sim 473 \text{ cm}^{-1}$. These peaks indicated the shell-core structure of hematite (Chernyshova et al., 2007). Throughout the fitted peak, the characteristics of peaks can explain the transformation shift of the Fe-O band. The E_u band absorption fit to a shell/core pair at $\sim 440/\sim 473 \text{ cm}^{-1}$, the intensity of shell peak ($\sim 440 \text{ cm}^{-1}$) increases within higher temperature, indicating greater particle size. Furthermore, the redshift of shell peaks from 443 cm^{-1} to 440 cm^{-1} and broader peaks

indicated that the Fe-O band was weakened by lattice disorder (Chernyshova et al., 2007). Meanwhile, the FWHM values of the core peak ($\sim 473 \text{ cm}^{-1}$) decrease, indicating the finer crystallinity of hematite and greater particle size. Table 4 provides the fitting shell/core pair calculation at $\sim 440/\sim 473 \text{ cm}^{-1}$ peaks.

3.5. Diffuse Reflectance spectroscopy (DRS)

The characterization using UV-Vis DRS was conducted to observe the electronic transitions that occurred in samples. Figure 5 presents the UV-Vis DRS spectra of the hematite samples calcined at different temperatures in the range of 600°C - 1100°C and Table 5 indicates the electronic transitions of each peak. The spectra present the characteristic of hematite with a redshift to a higher wavelength throughout the calcination temperature increases. The peak shift occurs in the $^6A_1 \rightarrow ^4T_2$ electronic transition around the 630 - 780 nm wavelength from the smaller to the larger wavelength. The wavelength shift was caused by particle size and the shape discrepancies of the material. The smaller size of the material will absorb a smaller wavelength (Sklute et al., 2017; Zhang et al., 2013; Cornell and Schwertmann, 2003). A study conducted by (Cornell and Schwertmann, 2003) reported that differences in particle shape would affect the intensity of the peaks in the spectra. For example, an asymmetric circular-shaped particle will have a high reflectance value compared to symmetrical particles. This shape results in a difference in the hematite color, as shown in Figure 3a. While (Sklute et al., 2017) reported a shift in the wavelength value due to differences in the shape of the hematite particles.

In line with the results of TEM observation, as the calcination temperature increases, the shape of the particle will shift from an asymmetric circular shape to an octahedral shape which is more symmetrical. Furthermore, the particle size increases with the increase in calcination temperature. The UV-Vis DRS spectra observations indicated a tendency of decreasing intensity and a shift in the low wavelength value to a higher one resulting in a color change from yellowish-red to purplish-red.

3.6. Fe K-edge XANES

The characterization using XANES was carried out to obtain specific information from the iron atoms contained in the hematite sample, particularly the local atomic structure, atomic oxidation number, and energy transition in the atom (Bora et al., 2013). Figure 6a shows the

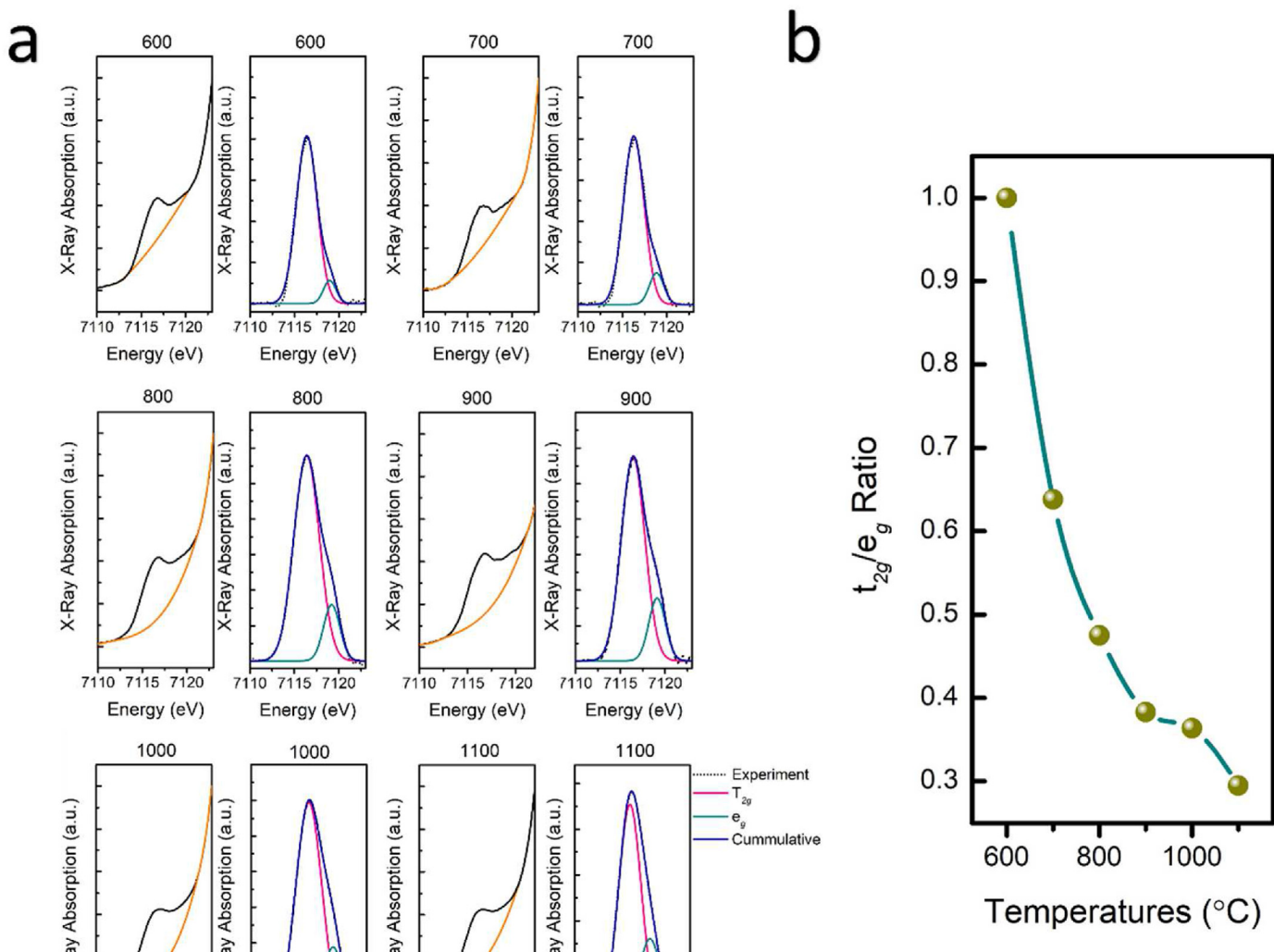


Figure 7. (a) Baseline plot (Left) with Pre-edge deconvolution and (b) t_{2g}/e_g ratio of hematite at temperature 600 °C–1100 °C.

XANES spectra of the Fe atom and the spectra of its first derivatives (Figure 6b). Based on the analysis results, all samples have an iron oxidation number of 3+, which is indicated by a peak at the energy E_0 of 7126.6 eV. E_0 defines the ionization threshold to the continuum state and can assign the oxidation state of materials (Fdez-Gubieda et al., 2016). Thus, this energy is specific energy indicating the oxidation level of the Fe^{3+} ion, while the lower oxidation state of an element will have a lower energy peak. The derivative spectra of samples also showed the K absorption associated with $1s \rightarrow 4s$ transition at E_0 7122.8 eV associated with $\text{Fe}^{3+}/\Sigma\text{Fe}$ (Mastelaro and Zanotto, 2018).

Other information that can be used is pre-edge spectra which can show a $1s \rightarrow 3d$ transition via the T_{2g}/e_g ratio (Δ_O) octahedral symmetry of the hematite. Based on the deconvolved pre-edge spectra in Figure 7, the hematite samples with higher combustion temperatures tend to have a lower t_{2g}/e_g ratio compared to those with lower combustion temperatures. This shows a distortion of the octahedral geometry of the hematite due to the combustion treatment (Ilmi et al., 2020; Nurdini et al., 2020; Bora et al., 2013). Furthermore, Pailhe et al. (2008) reported that the high calcined temperature of hematite leads to the distorted octahedral site of Fe^{3+} and is linked to the crystallite size. Hematite with a larger

crystallite size tended to have a more distorted octahedral site than hematite with a smaller crystallite size.

4. Discussions

Hematite that undergoes heating treatment at high temperatures produces a darker color compared to those treated at lower temperatures. This phenomenon can be explained in Figure 8. Based on various instrumentations' results, hematite at higher calcined temperatures results in shorter lattice parameter changes, especially on the c axis. Furthermore, the observation of $1s \rightarrow 3d$ transition shows that the value of Δ_O is getting smaller due to the distortion of the octahedral symmetry of hematite—the Δ_O value changes cause a shift in the absorbed energy of the polychromatic light. The value of Δ_O has a value that is inversely proportional to the wavelength, so if the value of Δ_O is small, it will absorb large wavelengths. In the case of hematite burned at a lower temperature (600 °C), the Δ_O value possessed by the material will absorb light at a green wavelength (~490 nm), then transmit its complementary color, red. Meanwhile, hematite burned at a higher temperature (1100 °C) has a smaller Δ_O . Thus, it will absorb light at a wavelength larger than

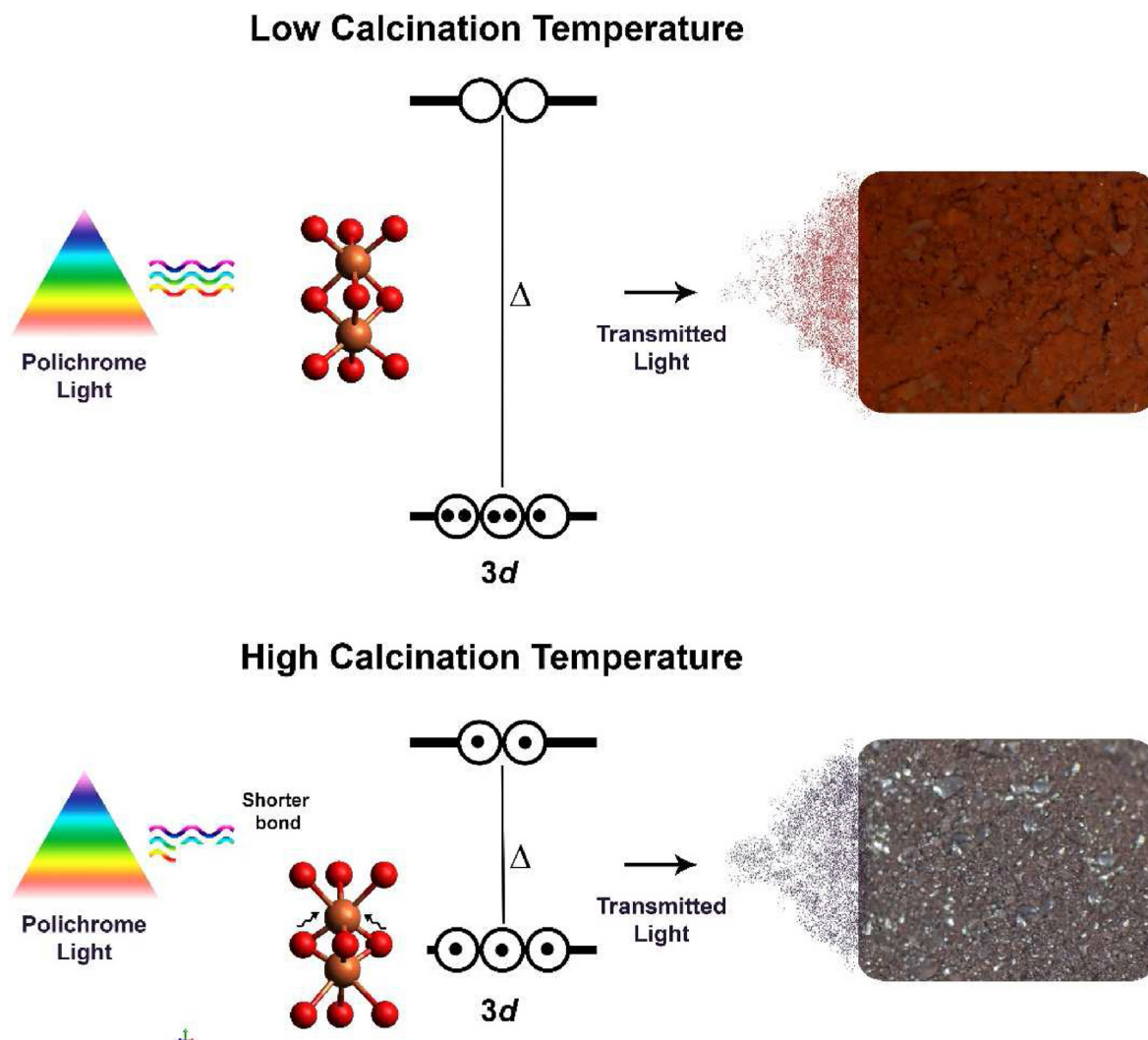


Figure 8. The illustration of the electronic properties of hematite that change the absorption of visible wavelength resulted in the color shift from red to purple.

green, yellow (~ 580 nm) and show a complementary purple color. In the laboratory, synthesized hematite using the precipitation method from iron salt precursors and calcined at a high temperature between 600 °C and 1100 °C showed results that heating treatment to the red hematite can be used as a reference to support the archaeological theory that prehistoric humans did the heating process on red ochre as a natural pigment, then applied in rock art. However, this finding needs to be confirmed using natural pigment (red ochre) used by prehistoric humans. Natural red pigment (red ochre) commonly contains a mixture between hematite and other minerals, including clay and silica, which may affect the heating treatment results in the pigment color.

5. Conclusions

In summary, we have thoroughly investigated the color transformation of hematite as a function of sintering temperature using detailed multi-characterization techniques, i.e., XRD, TEM, Raman spectroscopy, FTIR, UV-Vis DRS, and Fe K-edge XANES. Aside from common explanations that correlate the hematite's color transformation to either particle size or crystallinity that increase gradually along with calcination temperature increase, herein, we demonstrated that electronic properties of hematite play a significant role in determining the color of hematite pigment. The high sintering temperature of hematite

can cause an octahedral distortion, which affects the hematite's electronic structure. In specific, the hematite treated at a higher temperature exhibited a lower energy for the $1s \rightarrow 3d$ transition leading to the redshift of the adsorbed light that produced a purple color. The XRD, Raman spectroscopy, and FTIR results indicated that purple hematite possessed high crystallinity materials. Furthermore, the TEM observation displayed a dense and octahedral shape with a larger particle size owned by purple hematite.

The color shift occurred gradually from bright red, dark red, and purple starting at 1000 °C of calcination temperature. This research is fundamental research before observing natural pigment samples used in prehistoric rock art. Thus, when using natural samples consisting of a mixture of hematite, clay, and silica, the effect of impurities from natural samples can be explicitly observed. Our finding supports the hypothesis that prehistoric humans might obtain a purple hematite pigment via a heating treatment that previously was still speculated.

Declarations

Author contribution statement

Nadya Nurdini: Conceived and designed the experiments; Performed the experiments; Analyzed and interpreted the data; Wrote the paper.

Moh. Mualliful Ilmi, Evi Maryanti, Pindi Setiawan: Conceived and designed the experiments; Analyzed and interpreted the data.

Grandprix Thomryes Marth Kadja, Ismunandar: Conceived and designed the experiments; Analyzed and interpreted the data; Contributed reagents, materials, analysis tools or data; Wrote the paper.

Funding statement

This work was funded by the Ministry of Research and Technology (Kemenristek)/National Research and Innovation Agency (BRIN) of the Republic of Indonesia through the PMDSU Research Funding. MMI and NN thank the PMDSU scholarship from the Ministry of Education and Culture, the Republic of Indonesia. EM is grateful to the LPDP (Indonesia Endowment Fund for Education) scholarship from the Ministry of Finance, the Republic of Indonesia.

Data availability statement

Data included in article/supplementary material/referenced in article.

Declaration of interests statement

The authors declare no conflict of interest.

Additional information

No additional information is available for this paper.

Acknowledgements

We acknowledge the Synchrotron Light Research Institute (SLRI) for the supervision of beamtime, and we would like to thank the staff of beamline 1.1W for their assistance.

References

- Almeida, T.P., Fay, M., Zhu, Y., Brown, P.D., 2009. Process map for the hydrothermal synthesis of α -Fe₂O₃ nanorods. *J. Phys. Chem.* 113, 18689–18698.
- Aubert, M., Setiawan, P., Oktaviana, A.A., Brumm, A., Sulistyarto, P.H., Saptomo, E.W., Setiawan, B., Ma'rifat, T.A., Wahyuno, V.N., Atmoko, F.T., Zhao, J.-X., Huntley, J.P.S.C., Taqon, D.L., Howard, H.E.A., Brand, 2018. Paleolithic cave art in Borneo. *Nature* 564, 254–257.
- Aubert, M., Lebe, R., Oktaviana, A.A., Tang, M., Burhan, B., Hamrullah, Jusdi, A., Abdullah, Hakim, B., Zhao, J.-X., Gerla, I.M., Sulistyarto, P.H., Sardi, R., Brumm, A., 2019. Earliest hunting scene in prehistoric art. *Nature* 576, 442–445.
- Bora, D.K., Braun, A., Constable, E.C., "In Rust we trust", 2013. Hematite—the prospective inorganic backbone for artificial photosynthesis. *Energy Environ. Sci.* 6, 407–425.
- Castagnotto, E., Locardi, F., Slimani, S., Peddis, D., Gaggero, L., Ferretti, M., 2021. Characterization of the Caput Mortuum purple hematite pigment and synthesis of a modern analogue. *Dyes Pigments* 185 (A), 108881.
- Chalmin, E., Huntley, J., 2018. Characterizing rock art pigments. In: David, B., McNiven, I.J. (Eds.), *The Oxford Handbook of the Archaeology and Anthropology of Rock Art*. Oxford University Press.
- Chalmin, E., Menu, M., Vignaud, C., 2003. Analysis of rock art painting and technology of Palaeolithic painters. *Meas. Sci. Technol.* 14, 1590–1597.
- Chalmin, E., Vignaud, C., Menu, M., 2004. Palaeolithic painting matter: natural or heat-treated pigment? *Appl. Phys. A: Mater. Sci. Process.* 79, 187–191.
- Chalmin, E., Vignaud, C., Salomon, H., Farges, F., Susini, J., Menu, M., 2006. Minerals discovered in paleolithic black pigments by transmission electron microscopy and micro-X-ray absorption near-edge structure. *Appl. Phys. A: Mater. Sci. Process.* 83, 213–218.
- Chernysheva, I.V., Hochella Jr., M.F., Madden, A.S., 2007. Size-dependent structural transformations of hematite nanoparticles. 1. Phase transition. *Phys. Chem. Chem. Phys.* 9, 1736–1750.
- Chukanov, N.V., Chervonnyi, A.D., 2016. Some general aspects of the application of IR spectroscopy to the investigation of minerals. *Infrared Spectroscopy of Minerals and Related Compounds*, 1st. Springer Cham.
- Cornell, R.M., Schwerdtmann, U., 2003. *The Iron Oxide: Structures, Properties, Reactions, Occurrences and Uses*, second ed. John Wiley & Sons, Weinheim.
- de Oliveira, L.F.C., Edwards, H.G.M., Frost, R.L., Kloprogge, J.T., Middleton, P.S., 2002. Caput mortuum: spectroscopic and structural studies of an ancient pigment. *Analyst* 127 (4), 536–541.
- Elias, M., Chartier, C., Prévot, G., Garay, H., Vignaud, C., 2006. The colour of ochres explained by their composition. *Mater. Sci. Eng. B* 127, 70–80.
- Faivre, D., 2016. *Iron Oxides from Nature to Applications*. John Wiley & Sons, Weinheim.
- Fdez-Gubieda, M.S., García-Prieto, A., Alonso, J., Meneghini, C., 2016. X-ray Absorption fine Structure Spectroscopy in Fe Oxides and Oxyhydroxides in D. Faivre. *Iron Oxides from Nature to Applications*. John Wiley & Sons, Weinheim.
- Fouad, D.E., Zhang, C., El-Didamony, H., Yingnan, L., Mekuria, T.D., Shah, A.H., 2019. Improved size, morphology and crystallinity of hematite (α -Fe₂O₃) nanoparticles synthesized via the precipitation route using ferric sulfate precursor. *Results Phys.* 12, 1253–1261.
- Heaney, P.J., Oxman, M.J., Chen, S.A., 2020. A structural study of size-dependent lattice variation: in situ X-ray diffraction of the growth of goethite nanoparticles from 2-line ferrihydrite. *Am. Mineral.* 105, 652–663.
- Hunt, A., Thomas, P., James, D., David, B., Geneste, J.-M., Delannoy, J.-J., Stuart, B., 2016. The characterisation of pigments used in X-ray rock art at Dalakngalarr 1, central-western Arnhem Land. *Microchem. J.* 126, 524–529.
- Huntley, J., Brand, H., Aubert, M., Morwood, M.J., 2014. The first Australian Synchrotron powder diffraction analysis of pigment from a Wandjina motif in the Kimberley, Western Australia. *Aust. Archaeol.* 78, 33–38.
- Huntley, J., Aubert, M., Ross, J., Brand, H., Morwood, M.J., 2015. One colour (at least) two minerals: a study of mulberry rock art pigment and a mulberry pigment 'quarry' from the Kimberley, Northern Australia. *Archaeometry* 57, 77–99.
- Ilmi, M.M., Nurdini, N., Maryanti, E., Saiyasombat, C., Setiawan, P., Kadja, G.T.M., Ismunandar, 2020. Multi-analytical characterization of prehistoric rock art pigments from Liang Karim cave, Sangkulirang-Mangkalihat site, East Kalimantan, Indonesia. *Microchem. J.* Article 104738.
- Ilmi, M.M., Nurdini, N., Maryanti, E., Saiyasombat, C., Setiawan, P., Kadja, G.T.M., Ismunandar, 2021a. A multianalytical investigation of the physicochemical properties of white rock art pigments at the Nali and Tene Koro sites, Lembata, East Nusa Tenggara, Indonesia. *J. Archaeol. Sci.: Rep.* 41, 103326.
- Ilmi, M.M., Maryanti, E., Nurdini, N., Setiawan, P., Kadja, G.T.M., Ismunandar, 2021b. A review of radiometric dating and pigment characterizations of rock art in Indonesia. *Archaeol. Anthropol. Sci.* 13, 120.
- Iriarte, E., Foyo, A., Sánchez, M.A., Tomillo, C., 2009. The origin and geochemical characterization of red ochres from the Tito Bustillo and Monte Castillo Caves (Northern Spain). *Archaeometry* 51 (2), 231–251.
- Jubb, A.M., Allen, H.C., 2010. Vibrational spectroscopic characterization of hematite, maghemite, and magnetite thin films produced by vapor deposition. *ACS Appl. Mater. Interfaces* 2 (10), 2804–2812.
- Kinebuchi, I., Kyono, A., 2021. Study on magnetite oxidation using synchrotron X-ray diffraction and X-ray absorption spectroscopy: Vacancy ordering transition in maghemite (γ -Fe₂O₃). *J. Mineral. Petrol. Sci.* 116, 211–219.
- Kubáňová, D., Kubíčková, L., Kmíć, T., Závěta, K., Nižnánský, D., Brázda, P., Klementová, M., Kohout, J., 2019. Hematite: Morin temperature of nanoparticles with different size. *J. Magn. Magn. Mater.* 475, 611–619.
- Kurniawan, R., Kadja, G.T.M., Setiawan, Burhan, B., Oktaviana, A.A., Rustan, Hakim, B., Aubert, M., Brumm, A., Ismunandar, 2019. Chemistry of prehistoric rock art pigments from the Indonesian island of Sulawesi. *Microchem. J.* 146, 227–233.
- Lassoued, A., Dkhil, B., Gadri, A., Ammar, S., 2017. Control of the shape and size of iron oxide (α -Fe₂O₃) nanoparticles synthesized through the chemical precipitation method. *Results Phys.* 7, 3007–3015.
- Lassoued, A., Lassoued, M.S., Dkhil, B., Ammar, S., Gadri, A., 2018. Synthesis, structural, morphological, optical and magnetic characterization of iron oxide (α -Fe₂O₃) nanoparticles by precipitation method: effect of varying the nature of precursor. *Phys. E Low-dimens. Syst. Nanostruct.* 97, 328–334.
- Longa-Avello, L., Pereyra-Zerpa, C., Casal-Ramos, J.A., Delvasto, P., 2017. Study of the calcination process of two limonitic iron ores between 250 °C and 950 °C. *Rev. Fac. Ing.* 26 (45), 33–45.
- Mansour, H., Letifi, H., Bargougui, R., Almeida-Didry, S.D., Negulescu, B., Autret-Lambert, C., Gadri, A., Ammar, S., 2017. Structural, optical, magnetic and electrical properties of hematite (α -Fe₂O₃) nanoparticles synthesized by two methods: polyol and precipitation. *Appl. Phys. A* 123, 787.
- Marshall, L.J., Williams, J.R., Almond, M.J., Atkinson, S.D.M., Cook, S.R.R., Matthews, W.W., Mortimore, J.J.I.L., 2005. Analysis of ochres from Clearwell Caves: the role of particle size in determining colour. *Spectrochim. Acta Mol. Biomol. Spectrosc.* 61 (1–2), 233–241.
- Marshall, C.P., Dufresne, W.J.B., Rufeldt, C.J., 2020. Polarized Raman spectra of hematite and assignment of external modes. *J. Raman Spectrosc.* 51 (9), 1522–1529.
- Mastelaro, V.R., Zanotto, E.D., 2018. X-ray absorption fine structure (XAFS) studies of oxide glasses-A 45 year overview. *Materials* 11, 204.
- Mastrotheodoros, G., Beltsios, K.G., Zacharias, N., 2010. Assessment of the production of antiquity pigments through experimental treatment of ochres and other iron based precursors. *Mediterr. Archaeol. Archaeometry* 10 (1), 37–59.
- McPeak, J., Pohl, M.D., von Nagy, C.L., Hurst, H., Rowe, M.W., Gutiérrez, E.F.P., Russ, J., 2013. Physicochemical study of black pigments in prehistoric paints from Oxtotitlán cave, Guerrero, Mexico. *ACS (Am. Chem. Soc.) Symp. Ser.* 1147 (7), 123–143.
- Miot, J., Etique, M., 2016. Formation and transformation of iron-bearing minerals by iron(II)-oxidizing and iron(III)-reducing bacteria. *Iron Oxides* 53–98 in D. Faivre. (2016). Iron oxides from nature to applications, John Wiley and Sons, Weinheim.
- Moldenhauer, H., Bayer, M., Debus, J., Nikolov, A., Brümmer, A., 2018. Raman scattering study of micrometer-sized spots of magnetite and hematite formed at 18CrNiMo7-6 screw rotor surfaces due to liquid-free, unsynchronized operation. *IOP Conf. Ser. Mater. Sci. Eng.* 425, 012016.
- Mondragón, M.A., Hernández-Padrón, G., Solís, C., del Real, A., Trespalacios-Quijano, R., Jiménez-Mu, C., Viramontes-Anzures, C., 2019. Multianalytical characterization of pigments from rock paintings in Guanajuato, Central México. *J. Archaeol. Sci.: Report* 26, 101912.

- Morales-Morales, J.A., 2017. Synthesis of hematite α -Fe₂O₃ nano powders by the controlled precipitation method. *Ciencia en Desarrollo* 8 (1), 99–107.
- Nurdini, N., Maryanti, E., Ilmi, M.M., Sayasombat, C., Setiawan, P., Kadja, G.T.M., Ismunandar, 2020. Physicochemical investigation of prehistoric rock art pigments in Tewet Cave, Sangkulirang-Mangkalihat site, East Kalimantan-Indonesia. *J. Archaeol. Sci.: Rep.* 31, 102345.
- Opuchovic, O., Kareiva, A., 2015. Historical hematite pigment: synthesis by an aqueous sol-gel method, characterization and application for the colouration of ceramic glazes. *Ceram. Int.* 41, 4504–4513.
- Pailhe, N., Wattiaux, A., Gaudon, M., Demouergues, A., 2008. Impact of structural features on pigment properties of α -Fe₂O₃ haematite. *J. Solid State Chem.* 181, 2697–2704.
- Parrish, W., Langford, J.I., 2006. Problems arising from the K_α doublet. In: Prince, E. (Ed.), *International Tables for Crystallography Volume C: Mathematical, Physical and Chemical Tables*. John Wiley & Sons, New York, pp. 62–63.
- Pomiès, M.-P., Menu, M., Vignaud, C., 1999. Red palaeolithic pigments: natural hematite or heated goethite? *Archaeometry* 41 (2), 275–285.
- Rachinger, W.A., 1948. A correction for the $\alpha_1\alpha_2$ doublet in the measurement of widths of X-ray diffraction lines. *J. Sci. Instrum.* 25, 254–255.
- Rafi, M.M., Ahmed, K.S.Z., Nazeer, K.P., Kumar, D.S., Thamilselvan, M., 2015. Synthesis, characterization and magnetic properties of hematite (α -Fe₂O₃) nanoparticles on polysaccharide templates and their antibacterial activity. *Appl. Nanosci.* 5, 515–520.
- Ravel, B., Newville, M., 2005. ATHENA, artemis, hephaestus: data analysis for X-ray absorption spectroscopy using IFEFFIT. *J. Synchrotron Radiat.* 12, 537–541.
- Rout, K., Mohapatra, M., Layek, S., Dash, A., Vermab, H.C., Anand, S., 2014. The influence of precursors on phase evolution of nano iron oxides/oxyhydroxides: optical and magnetic properties. *New J. Chem.* 38, 3492–3506.
- Salomon, H., Vignaud, C., Coquinot, Y., Beck, L., Stringer, C., Strivay, D., D'Errico, F., 2012. Selection and heating of colouring materials in the Mousterian level of Es-Skhul (c. 100 years BP, mount Carmel, Israel). *Archaeometry* 54, 698–722.
- Sklute, E.C., Kashyap, S., Dyar, M.D., Holde, J.F., Tague, T., Wang, P., Jaret, S.J., 2017. Spectral and morphological characteristics of synthetic nanoparticle iron (oxyhydr) oxides. *Phys. Chem. Miner.* 45 (1), 1–26.
- Sorescu, M., Xu, T., 2012. Particle size effects on the thermal behavior of hematite. *J. Therm. Anal. Calorim.* 107 (2), 463–469.
- Tadic, M., Trpkov, D., Kopanja, L., Vojnovic, S., Panjan, M., 2019. Hydrothermal synthesis of hematite (α -Fe₂O₃) nanoparticle forms: synthesis conditions, structure, particle shape analysis, cytotoxicity and magnetic properties. *J. Alloys Compd.* 792 (9), 599–609.
- Xu, S., Habib, A.H., Gee, S.H., Hong, Y.K., McHenry, M.E., 2015. Spin orientation, structure, morphology, and magnetic properties of hematite nanoparticles. *J. Appl. Phys.* 117, 17A315.
- Zhang, X., Niu, Y., Li, Y., Hou, X., Wang, Y., Bai, R., Zhao, J., 2013. Synthesis, optical and magnetic properties of α -Fe₂O₃ nanoparticles with various shapes. *Mater. Lett.* 99, 111–114.